Supplementary Information

Steady Rotation and Wall-Mediated Dynamics of Magnetic Janus Particles in Oscillating Fields

Amrutha Raghu[1], Kyle J. M. Bishop[2], and Bhuvnesh Bharti[1]

[1]Cain Department of Chemical Engineering, Louisiana State University, Baton Rouge, LA 70803, USA
[2]Department of Chemical Engineering, Columbia University, New York, NY 10027, USA

Contents

1 Magnetization data

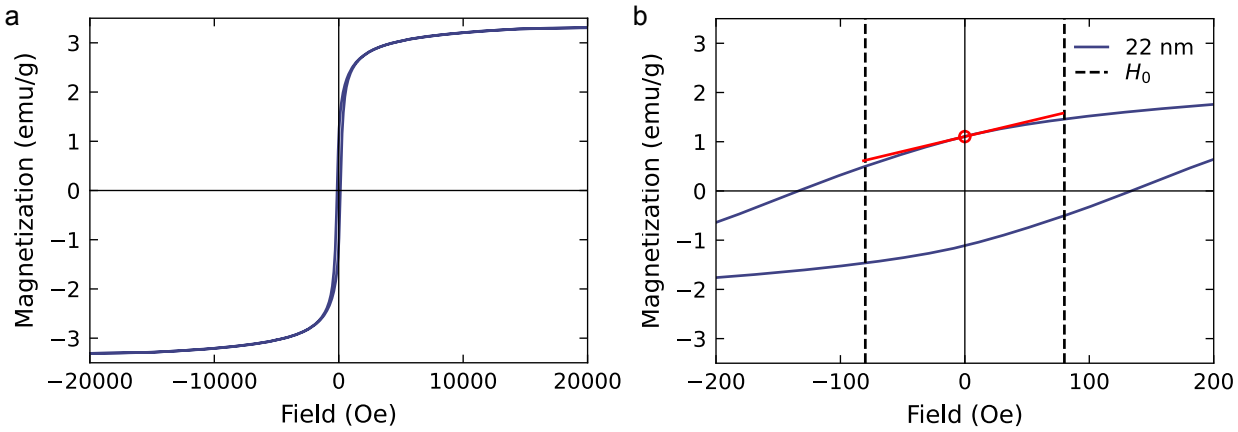

Figure S1: Vibrating-sample magnetometer (VSM) data showing specific magnetization versus applied field strength for 5 μm Janus spheres with a 22 nm iron coating. Plot (a) shows the full range of applied field strengths from $\pm 2 \times 10^4$ Oe; plot (b) focuses on the range of field strengths relevant to the experiment ± 80 Oe. The red marker denotes the remnant magnetization at zero field: 1.1 emu/g. The red line denotes slope of the magnetization-field curve at zero field: 0.0060 emu/g Oe. We multiply these quantities by the estimated mass of a single Janus sphere, $M = 7.5 \times 10^{-11}$ g, to estimate the permanent particle moment $m_\mathrm{p} = 8.3 \times 10^{-11}$ emu (8.3×10^{-14} A m^2) and the average polarizability $\alpha = 4.5 \times 10^{-13}$ emu/Oe (5.7×10^{-18} m^3).

2 Particle-substrate height measurement

As detailed in the Methods, optical microscopy is used to determine the location of the substrate by first focusing on patterned gold mask on the glass substrate (Fig. S2) and then adjusting the microscope stage along the z-direction by a prescribed distance.

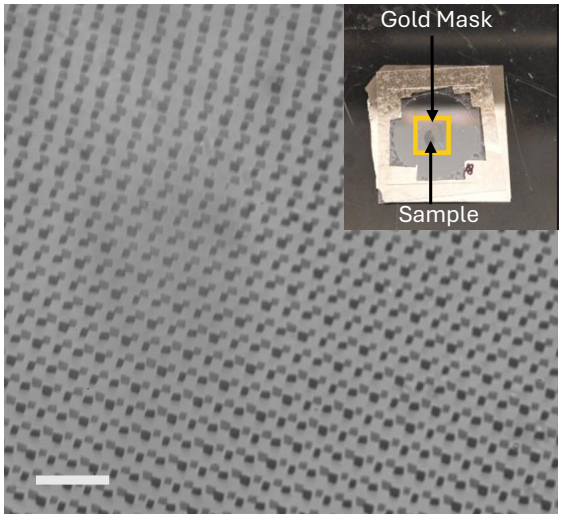

Figure S2: Bright-field microscopy image of the gold mask on the glass substrate. Scale bar is 50 μm. The inset shows an image of the Janus particle dispersion sealed between a glass cover-slip and the glass substrate above the gold mask (highlighted in yellow).

3 Particle sedimentation rate

We quantified the rate of particle sedimentation and find that it is slow compared to the experimental time scales. Magnetic Janus particles dispersed above the substrate were allowed to settle while being monitored by optical microscopy. Particles initially positioned in the focal plane take several hours to disappear via sedimentation. We measured the particle height from the substrate every 30 min to better estimate the settling rate (Fig. S3). The measured sedimentation velocity is $U \approx 5$ μm/hr (1×10^{-3} μm/s). Over the duration of a typical experiment (ca. 20 s), the resulting particle vertical displacement is negligible (ca. 0.03 μm), indicating that gravitational settling does not contribute appreciably to the observed particle dynamics.

These sedimentation experiments suggest that the average density of the magnetic Janus particles is very closely matched to their aqueous surroundings with an estimated density contrast $\Delta\rho \approx 9\eta U/2ga^2 \approx 0.1$ kg/m^3, where $\eta = 1$ mPa s, $g = 9.8$ m/s^2, and $a = 2.5$ μm.

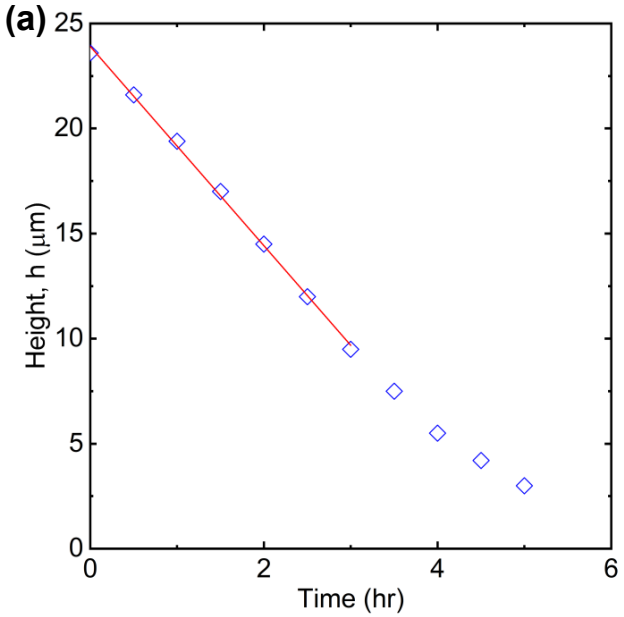

Figure S3: Sedimentation experiments. Particle height as a function of time measured using microscopy. The Janus particles were allowed to settle in the quiescent fluid, and the height of the particle was estimated by the difference in the focal plane of the particle and the underlying substrate. See Methods for further details.

4 Derivation of the dynamical model

We consider a spherical particle with radius a and magnetic moment $\mathbf{m}$ immersed in viscous fluid at a height h above a solid plane at $z = 0$ (Fig. S4). The sphere is subject to a AC magnetic field directed normal to the surface $\mathbf{H}(t) = H_0 \sin \omega t \, \mathbf{e}_z$. The particle's linear velocity $\mathbf{U}$ and angular velocity $\boldsymbol{\Omega}$ are governed by Newton's laws of rigid body motion

$$\frac{d}{dt}\left(M\mathbf{U}\right) = \sum_i \mathbf{F}_i \quad \text{and} \quad \frac{d}{dt}\left(\mathbf{I}\cdot\boldsymbol{\Omega}\right) = \sum_i \mathbf{T}_i \tag{1}$$

where $\mathbf{F}_i$ and $\mathbf{T}_i$ denote the force and torque of type i, M is the particle mass, and $\mathbf{I}$ is the inertia tensor. For a homogeneous sphere, the inertia tensor is isotropic and equal to $\mathbf{I} = I\boldsymbol{\delta}$ with $I = \frac{2}{5}Ma^2$.

Hydrodynamic Force & Torque. At low Reynolds number, the hydrodynamic force and torque on the sphere in a quiescent fluid are linearly related to the linear and angular velocity as

$$\begin{bmatrix}\mathbf{F}_\mathrm{h}\\ \mathbf{T}_\mathrm{h}\end{bmatrix} = -\begin{bmatrix}\mathbf{A} & \tilde{\mathbf{B}}\\ \mathbf{B} & \mathbf{C}\end{bmatrix}\cdot\begin{bmatrix}\mathbf{U}\\ \boldsymbol{\Omega}\end{bmatrix} \tag{2}$$

where $\mathbf{A}$, $\mathbf{B}$, etc. are components of the hydrodynamic resistance matrix.[1] For a solid sphere above a solid plane normal to the $\mathbf{e}_3$-direction, the components of the resistance matrix have the form

$$\begin{aligned}\mathbf{A} &= 6\pi\eta a\left[Y_A(\boldsymbol{\delta}-\mathbf{e}_z\mathbf{e}_z) + X_A\mathbf{e}_z\mathbf{e}_z\right]\\ \mathbf{B} = -\tilde{\mathbf{B}} &= 6\pi\eta a^2\left[Y_B\,\boldsymbol{\epsilon}\cdot\mathbf{e}_z\right]\\ \mathbf{C} &= 6\pi\eta a^3\left[Y_C(\boldsymbol{\delta}-\mathbf{e}_z\mathbf{e}_z) + X_C\mathbf{e}_z\mathbf{e}_z\right]\end{aligned} \tag{3}$$

where η is the fluid viscosity, $\boldsymbol{\delta}$ is the identity tensor, $\boldsymbol{\epsilon}$ is the Levi-Civita tensor, and $\mathbf{e}_i$ denote unit vectors in the i-direction. The resistance coefficients X_A, Y_A, Y_B, X_C, and Y_C depend on the dimensionless surface separation $\xi = (h-a)/a$ as described by semi-analytical solutions.[2–6]

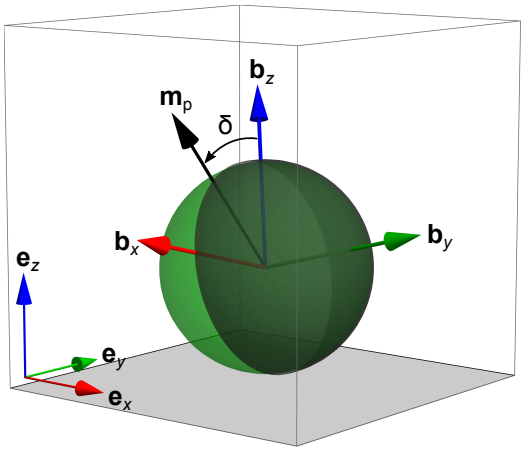

Figure S4: Schematic illustration of a Janus sphere above a plane wall illustrating the lab frame characterized by unit vectors $\mathbf{e}_y, \mathbf{e}_y, \mathbf{e}_z$ and the particle frame characterized by unit vectors $\mathbf{b}_y, \mathbf{b}_y, \mathbf{b}_z$. The director $\mathbf{d}$ of the Janus cap (grey) points along the $\mathbf{b}_y$ direction.

Magnetic Torque. The magnetic field $\mathbf{H}(t) = H_z(t)\mathbf{e}_z$ acts on the particle's magnetic moment $\mathbf{m}$ to generate a magnetic torque

$$\mathbf{T}_\mathrm{m} = \mu_0(\mathbf{m} \times \mathbf{H}) = \mu_0 H_z \left(m_y \mathbf{e}_x - m_x \mathbf{e}_y\right) \tag{4}$$

where μ_0 is the vacuum permeability. The spatially uniform field generates no magnetic force: $\mathbf{F}_\mathrm{m} = 0$.

Magnetic Moment. Based on vibrating-sample magnetometer (VSM) data (see Section 1), the particle's magnetic moment $\mathbf{m}$ has two primary contributions: a permanent moment $\mathbf{m}_\mathrm{p}$ and an induced moment $\mathbf{m}_\mathrm{i}$. The permanent moment is constant in the particle reference frame, changing in the lab frame only via particle rotation. Using particle-fixed unit vectors $\mathbf{b}_x$, $\mathbf{b}_y$, $\mathbf{b}_z$, the permanent moment is expressed as

$$\mathbf{m}_\mathrm{p} = m_x^\mathrm{p}\,\mathbf{b}_x + m_y^\mathrm{p}\,\mathbf{b}_y + m_z^\mathrm{p}\,\mathbf{b}_z \tag{5}$$

The induced moment $\mathbf{m}_\mathrm{i}$ relaxes to an asymptotic value proportional to the applied field $\boldsymbol{\alpha} \cdot \mathbf{H}$, where $\boldsymbol{\alpha}$ is the magnetic polarizability tensor. Because this tensor is symmetric, its eigenvectors are orthogonal. We chose the particle-fixed unit vectors to coincide with these principal directions of $\boldsymbol{\alpha}$ such that

$$\boldsymbol{\alpha} = \alpha_x \mathbf{b}_x\mathbf{b}_x + \alpha_y \mathbf{b}_y\mathbf{b}_y + \alpha_z \mathbf{b}_z\mathbf{b}_z \tag{6}$$

where α_i is the polarizability along the i^th direction of the particle. The unit vectors $\mathbf{b}_x$, $\mathbf{b}_y$, $\mathbf{b}_z$ are assigned such that $\alpha_y < \alpha_x < \alpha_z$. We assume that the induced moment relaxes along these principal directions with rate constants k_x, k_y, and k_z as described by the relaxation rate tensor $\mathbf{k}$

$$\mathbf{k} = k_x \mathbf{b}_x\mathbf{b}_x + k_y \mathbf{b}_y\mathbf{b}_y + k_z \mathbf{b}_z\mathbf{b}_z \tag{7}$$

The induced moment $\mathbf{m}_\mathrm{i}$ changes in time due to both *internal* relaxation and *external* rotation as

$$\frac{d\mathbf{m}_\mathrm{i}}{dt} = -\mathbf{k} \cdot (\mathbf{m}_\mathrm{i} - \boldsymbol{\alpha} \cdot \mathbf{H}) + \boldsymbol{\Omega} \times \mathbf{m}_\mathrm{i} \tag{8}$$

Particle Rotation. The orientation of the particle is parameterized by the Euler angles $\mathbf{u} = [\phi, \theta, \psi]^T$ using the 323 (zyz) rotation sequence characterized by the rotation matrix

$$R_{323}(\mathbf{u}) = R_z(\phi)R_y(\theta)R_z(\psi) = \begin{bmatrix} c_\phi c_\theta c_\psi - s_\phi s_\psi & c_\phi c_\theta s_\psi + s_\phi c_\psi & -c_\phi s_\theta \\ -s_\phi c_\theta c_\psi - c_\phi s_\psi & -s_\phi c_\theta s_\psi + c_\phi c_\psi & s_\phi s_\theta \\ s_\theta c_\psi & s_\theta s_\psi & c_\theta \end{bmatrix} \tag{9}$$

where $R_i(\phi)$ denotes a coordinate rotation by ϕ about the i-direction, and $s_x = \sin x$ and $c_x = \cos x$.[7] A vector $\mathbf{v} = [v_x, v_y, v_z]^T$ in the lab frame $(\mathbf{e}_x, \mathbf{e}_y, \mathbf{e}_z)$ is related to the same vector $\mathbf{v}' = [v'_x, v'_y, v'_z]^T$ in the particle frame $(\mathbf{b}_x, \mathbf{b}_y, \mathbf{b}_z)$ as $\mathbf{v}' = R_{323}\mathbf{v}$. Similarly, a tensor $\boldsymbol{\tau}$ in the lab frame is related to the same tensor $\boldsymbol{\tau}'$ in the particle frame as $\boldsymbol{\tau}' = R_{323}\boldsymbol{\tau}R_{323}^T$. The Euler angle rates $\dot{\mathbf{u}}$ are related to the angular velocity as $\boldsymbol{\Omega} = E_{323}(\mathbf{u})\dot{\mathbf{u}}$, where $E_{323}(\mathbf{u})$ is the Euler angle rate matrix

$$E_{323}(\mathbf{u}) = \begin{bmatrix} s_\theta c_\psi & -s_\psi & 0 \\ s_\theta s_\psi & c_\psi & 0 \\ c_\theta & 0 & 1 \end{bmatrix} \tag{10}$$

Similarly, the particle position $\mathbf{x}_\mathrm{p}$ is related to the linear velocity as $\dot{\mathbf{x}}_\mathrm{p} = \mathbf{U}$. Together, these equations can be integrated to determine the transient particle position $\mathbf{x}_p(t)$, orientation $\mathbf{u}(t)$, and induced moment $\mathbf{m}_\mathrm{i}$.

Non-dimensionization. It is convenient to non-dimensionalize the above equations using the following characteristic scales

$$\begin{aligned} &\text{moment:} \quad m_{\mathrm{p}} \qquad \text{field:} \quad H_0 \qquad\qquad \text{torque:} \quad \mu_0 m_{\mathrm{p}} H_0 \\ &\text{length:} \quad a \qquad\quad \text{rate:} \quad \omega_0 = \frac{\mu_0 m_{\mathrm{p}} H_0}{6\pi\eta a^3} \qquad \text{time:} \quad \omega_0^{-1} \end{aligned} \tag{11}$$

where ω_0 is a characteristic rate for field-driven particle rotation. Below, we use the same notation to refer to dimensionless quantities, which corresponds to setting the characteristic scales to unity in the dynamical equations above (e.g., $a \to 1$).

4.1 1D rotation about the y-axis

The above model simplifies considerably when the particle is constrained to rotate about a single axis. Assuming mirror symmetry about the y-direction, we set the Euler angles ψ and ϕ, the moments $m_{\mathrm{i}y}$ and $m_{\mathrm{p}y}$, and the angular velocities Ω_x and Ω_z to zero .

The remaining Euler angle $\theta(t)$ is governed by the dimensionless dynamics

$$\varepsilon\dot{\Omega}_y = -\frac{1}{Y_c}\Omega_y - (m_x^{\mathrm{i}} + m_x^{\mathrm{p}}\cos\theta + m_y^{\mathrm{p}}\sin\theta)\sin\omega t \quad \text{and} \quad \dot{\theta} = \Omega_y \tag{12}$$

where $\varepsilon = \mu_0 m_{\mathrm{p}} H_0/6\pi\eta a^3 \ll 1$ is a small inertia parameter, and $Y_c = (Y_A Y_C - Y_B^2)/Y_A$ is the mobility coefficient for particle rotation about the y-direction, which depends on the surface separation $\xi = (h-a)/a$ (Fig. S5a). While the mobility coefficient can be incorporated into the rate scale ω_0 to further simplify the equation, this choice obscures the role of the surface separation in influencing the particle dynamics.

The particle position $\mathbf{x}_{\mathrm{p}}(t)$ evolves as

$$\dot{\mathbf{x}}_{\mathrm{p}} = \mathbf{U} = \frac{Y_B}{Y_A}\Omega_y \mathbf{e}_x \tag{13}$$

where the ratio Y_B/Y_A is a positive constant characterizing the strength of rotation translation coupling. This ratio—sometimes known as the traction[8] and denoted κ in prior work[9,10]—varies from zero when the particle is far from the surface and approaches an asymptotic value of $1/4$ as the surface separation tends to zero (Fig. S5b).

Finally, the induced moment $\mathbf{m}_{\mathrm{i}}(t)$ is governed by the dimensionless equations

$$\begin{aligned} \dot{m}_x^{\mathrm{i}} &= \Omega_y m_z^{\mathrm{i}} + \tfrac{1}{2}\left(-(k_z+k_x)m_x^{\mathrm{i}} + (k_z-k_x)m_x^{\mathrm{i}}\cos 2\theta - (k_z-k_x)m_z^{\mathrm{i}}\sin 2\theta\right) \\ &\quad + \tfrac{1}{2}(k_z\alpha_z - k_x\alpha_x)\sin 2\theta\,\sin\omega t \\ \dot{m}_z^{\mathrm{i}} &= -\Omega_y m_x^{\mathrm{i}} + \tfrac{1}{2}\left(-(k_z+k_x)m_z^{\mathrm{i}} - (k_z-k_x)m_x^{\mathrm{i}}\sin 2\theta - (k_z-k_z)m_z^{\mathrm{i}}\cos 2\theta\right) \\ &\quad + \tfrac{1}{2}\big((k_z\alpha_z + k_x\alpha_x) + (k_z\alpha_z - k_x\alpha_x)\cos 2\theta\big)\,\sin\omega t \end{aligned} \tag{14}$$

Together, equations (12)–(14) describe the transient position and orientation of the particle.

4.2 Parameter estimates

To guide the analysis of the model, we use the experiment conditions and observations to estimate the relative magnitude of the many parameters. Some of these parameters are specified or known: the particle radius $a = 2.5$ μm; the applied field strength $\mu_0 H_0 = 8$ mT, the fluid viscosity $\eta = 1$ mPa s, the particle mass $M = 7.5 \times 10^{-14}$ kg (based on 20 nm of chromium and 22 nm

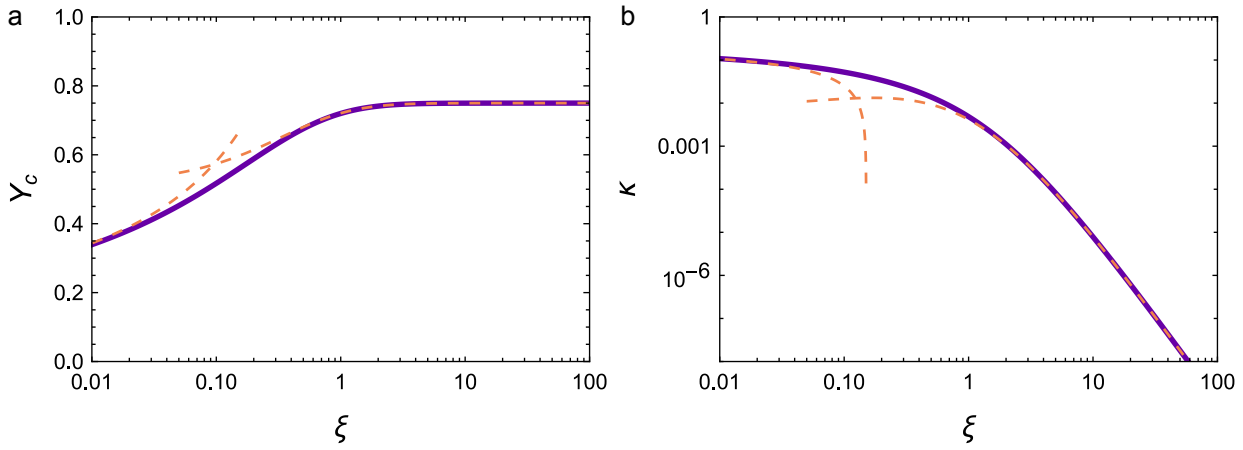

Figure S5: Sphere-plane mobility coefficients as a function of the scaled surface separation $\xi = (h - a)/a$. (a) Rotational mobility coefficient Y_c for a sphere subject to a torque perpendicular to the surface normal. The dashed curves show asymptotic approximations for small and large separations.[3] (b) Surface traction κ describing the strength of rotation-translation coupling. The dashed curves show asymptotic approximations for small and large separations.[3]

of iron onto a polystyrene core). Others are approximated from independent measurements: the permanent moment $m_\mathrm{p} \approx 8.3 \times 10^{-14}$ A m^2 and the average polarizability $\alpha \approx 5.7 \times 10^{-18}$ m^3 (see Fig. S1). With these estimates, the characteristic relaxation rate for magnetic rotation is $\omega_0 = \mu_0 m_\mathrm{p} H_0 / 6\pi\eta a^3 \approx 2200$ rad/s (or 360 Hz). The characteristic ratio between the field-induced moment and the permanent moment is $\alpha H_0 / m_\mathrm{p} \approx 0.44$.

In the rolling regime ($h \approx a$), the frequency-dependent rolling speed of Figure 2B suggests a phase-locked frequency window, in which the particle rotates in synchrony with the oscillating field (one particle revolution per cycle, $\Omega = \omega$). In dimensional units, the above model suggests that $U = \kappa a \omega$ under this assumption, where $\kappa = Y_B / Y_C$ is the traction. The fitted slope of experimental data for U vs. ω is 0.085 μm, which corresponds to a traction $\kappa \approx 0.034$. Based on the theoretical relationship between traction κ and surface separation ξ for the sphere-plane geometry (Fig. S5b), this estimate suggests a surface separation $\xi \approx 0.23$ (0.59 μm), which is physically reasonable. With this estimate, the relevant mobility coefficient for particle rotation parallel to the surface is $Y_c \approx 0.61$, which is not much smaller than its asymptotic value $Y_c \to 3/4$ for large surface separations $h \to \infty$.

The critical frequency ω_c above which synchronized particle rotation breaks is approximately $\omega_\mathrm{c}/2\pi \approx 47$ Hz from the data in Figure 2B. This value corresponds to a dimensionless frequency ratio of $\omega_\mathrm{c}/\omega_0 \approx 0.13$. The internal relaxation rates k_x, k_y, k_z are largely unknown; however, we will assume that they are considerably faster than the driving frequency ω and the rotational relaxation rate ω_0. Moreover, we will assume isotropic relaxation with $k_x = k_y = k_z = k$ to further simplify the analysis. Finally, while the average polarizability $\alpha = \frac{1}{3}(\alpha_x + \alpha_y + \alpha_z)$ is estimated from VSM data, the magnitude of any anisotropy is less clearly established. For the Janus cap geometry (with director $\mathbf{d}$ parallel to the $\mathbf{b}_y$ direction of the particle), it is often the case that $\alpha_y < \alpha_x \approx \alpha_z$: larger moments are induced perpendicular to the Janus director than along the parallel direction. For rotation about the director (as observed in experiments on rolling particles), the anisotropy $\alpha_z - \alpha_x \neq 0$ will become relevant. We assume this anisotropy is small compared to the average polarizability.

5 1D rolling in an oscillating field

Here, we consider a simplified model for 1D particle rotation in an oscillating field. Starting from equations (12)–(14), we neglect inertial effects $\varepsilon \to 0$ and assume instantaneous, isotropic relaxation $k \to \infty$. The resulting dimensionless equation for the particle orientation is

$$\dot{\theta} = \Omega_y = -Y_c\Big(\tfrac{1}{2}(\alpha_z - \alpha_x)\sin 2\theta \sin\omega t + m_x^{\mathrm{p}}\cos\theta + m_y^{\mathrm{p}}\sin\theta\Big)\sin\omega t \tag{15}$$

To simplify the analysis of this equation, we introduce a new rescaled time $\tilde{t} = Y_c t$ and frequency $\tilde{\omega} = \omega/Y_c$. Introducing the polarizability difference $\Delta_{xz} = \frac{1}{2}(\alpha_z - \alpha_x) > 0$ and parameterizing the permanent moment as $m_x^{\mathrm{p}} = \sin\delta$ and $m_z^{\mathrm{p}} = \cos\delta$, this rescaled equation becomes

$$\frac{d\theta}{d\tilde{t}} = -\Delta_{xz}\sin 2\theta \sin^2\tilde{\omega}\tilde{t} - \sin(\delta+\theta)\sin\tilde{\omega}\tilde{t} \tag{16}$$

This equation depends on three parameters: (1) the small polarizability difference $\Delta_{xz} \ll 1$, (2) the driving frequency $\tilde{\omega}$, and (3) the orientation of the permanent moment δ.

Figure S6a presents a numerical phase diagram showing the time-averaged angular velocity $\langle\Omega_y\rangle$ as a function of the field frequency $\tilde{\omega}$ and moment orientation δ for $\Delta_{xz} = 0.01$. This data is obtained by numerical integration of equation (16) for 200 cycles and averaging the angular velocity over the last 100 cycles. For moment angles $0 < \delta < \pi/2$, the time-averaged velocity increases with frequency as $\langle\tilde{\Omega}_y\rangle = \omega$ up to a critical value $\tilde{\omega}_{\mathrm{c}}$, above which it falls sharply toward zero (Fig. S6b). Notably, the orientation of the permanent moment between the higher and lower polarizability directions—namely, α_z and α_x—selects a favored direction of rotation. Here, $\langle\Omega_y\rangle > 0$ for $0 < \delta < \pi/2$; however, the direction of rotation reverses for $-\pi/2 < \delta < 0$. Rotation about the y-axis (as opposed to the x-axis) is simply a consequence of our chosen coordinate system. This model predicts particle rotation about any direction in the plane of the surface as observed in experiment.

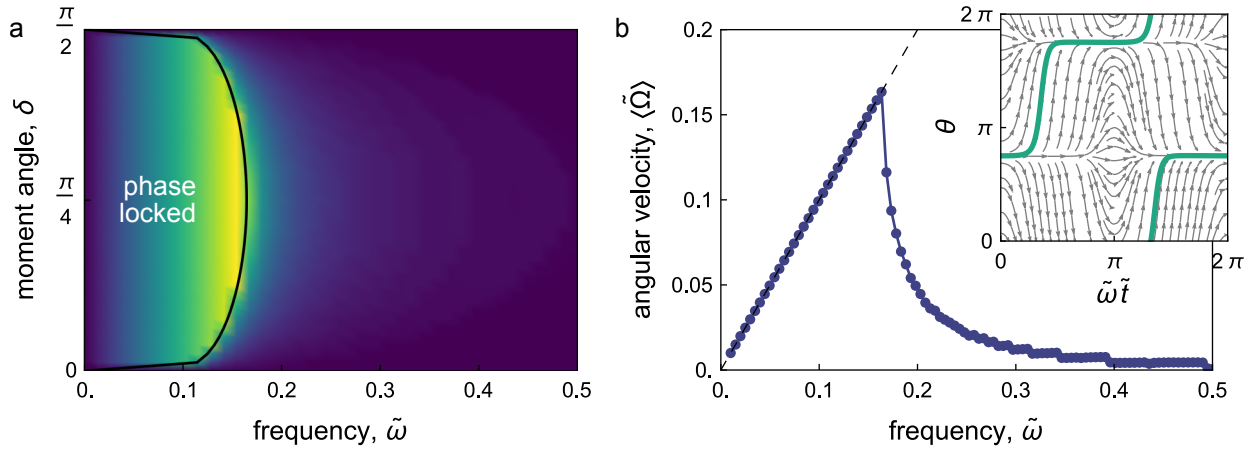

Figure S6: (a) Time-averaged velocity $\langle\tilde{\Omega}_y\rangle$ as a function of moment angle δ and frequency $\tilde{\omega}$ for a small polarizability difference $\epsilon_\alpha = 0.01$. The black curve separates phase-locked rolling regime ($\tilde{\omega} < \tilde{\omega}_{\mathrm{c}}(\delta)$) from the unlocked regime. (b) Time-averaged velocity $\langle\tilde{\Omega}_y\rangle$ as a function frequency $\tilde{\omega}$ for $\delta = \pi/4$ and $\Delta_{xz} = 0.01$. The dashed line denotes the phase-locked result $\langle\tilde{\Omega}_y\rangle = \tilde{\omega}$. The inset shows the phase portrait of the 2π-periodic solution for $\tilde{\omega} = 0.1$. All quantities are presented in dimensionless units: frequency and angular velocity are scaled by $Y_c\,\omega_0$.

No rolling for $\Delta_{xz} \to 0$. When the polarizabilities α_x and α_z are equal ($\Delta_{xz} \to 0$), the particle orientation θ oscillates in time with zero time-averaged velocity. In this limit, equation (16) can be integrated exactly to obtain

$$\theta(\tilde{t}) = -\delta \pm 2 \arctan\left[\exp\left(-\frac{\cos\tilde{\omega}\tilde{t}}{\tilde{\omega}}\right)\right] \tag{17}$$

For small frequencies ($\tilde{\omega} \ll 1$), the particle orientation rocks between $\theta + \delta \approx 0$ and π (or 0 and $-\pi$) as the permanent moment aligns with the external field.

Effect of particle height. In this 1D model, the height h of the particle above the solid substrate influences the mobility coefficient Y_c and thereby the scaled frequency $\tilde{\omega}$. The critical frequency ω_c below which the particle rotates in synchrony with the oscillating field depends on scaled surface separation as $\omega_c = Y_c(\xi)\tilde{\omega}_c(\Delta_{xz}, \delta)$. Figure S6a shows how the scaled critical frequency $\tilde{\omega}_c(\Delta_{xz}, \delta)$ depends on the moment angle δ for a constant $\Delta_{xz} = 0.01$. Similarly, Figure S7a shows how $\tilde{\omega}_c(\Delta_{xz}, \delta)$ depends on the polarizability difference Δ_{xz} for a constant $\delta = \pi/4$. For a constant applied frequency ω, increasing the surface separation acts to reduce the resistance to rotation thereby increasing the critical frequency and facilitating synchronized particle rotation in the driving field.

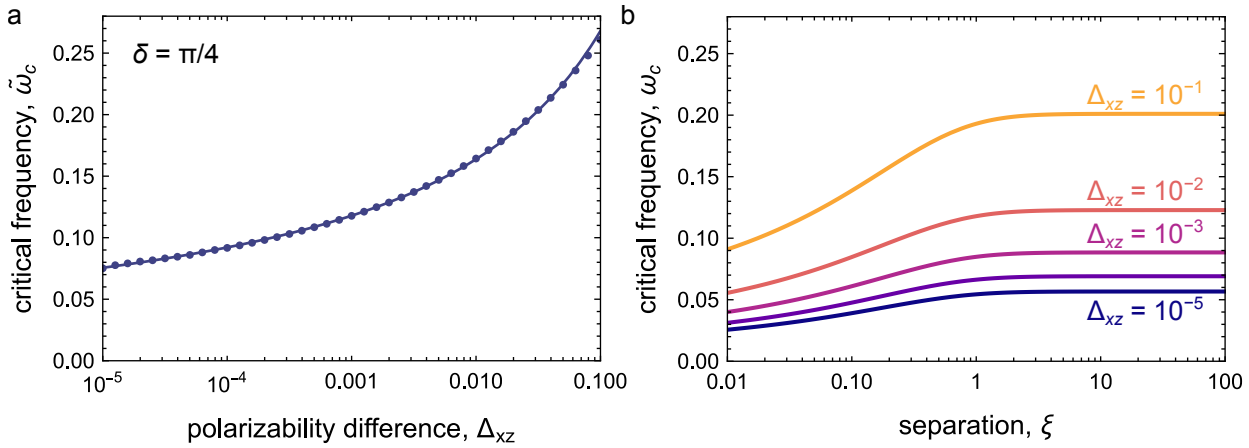

Figure S7: (a) Scaled critical frequency $\tilde{\omega}_c = \omega_c/Y_c$ vs. polarizability difference $\Delta_{xz} = \frac{1}{2}(\alpha_z - \alpha_x)$ computed numerically for the moment angle $\delta = \pi/4$. The solid curve shows a fitted interpolant: $\tilde{\omega}_c = (1.354 - 1.032 \ln \Delta_{xz})^{-1}$. (b) Critical frequency $\omega_c = Y_c(\xi)\tilde{\omega}_c(\Delta_{xz}, \delta)$ vs. scaled surface separation $\xi = h - 1$ for different values of the polarizability difference Δ_{xz} computed for the moment angle $\delta = \pi/4$.

6 Inertial effects are negligible

Using experiments and theory, Aronson and co-workers showed that a ferromagnetic sphere with radius a and permanent magnetic moment $\mathbf{m}_\mathrm{p}$ can—under certain conditions—rotate steadily in an oscillating magnetic field $\mathbf{H}(t) = H_0 \sin\omega t\, \mathbf{e}_z$.[11] Their dynamical model considers (i) the magnetic torque on the particle in the external field, (ii) the viscous resistance to rotation, and (iii) the particle's rotational inertia. Here, we parameterize the magnetic moment by the angle θ in the xz-plane as $\mathbf{m} = \sin\theta \mathbf{e}_x + \cos\theta \mathbf{e}_z$; the resulting magnetic torque is $\mathbf{T}_\mathrm{m} = \mathbf{m}_\mathrm{p} \times \mathbf{B} = -\mu_0 m_\mathrm{p} H_0 \sin\theta \sin\omega t\, \mathbf{e}_y$, where μ_0 is the vacuum permeability. The equation of motion for rotation about the y axis is

$$I\frac{d^2\theta}{dt^2} = -\zeta_\mathrm{r}\frac{d\theta}{dt} - \mu_0 m_\mathrm{p} H_0 \sin\theta \sin\omega t \tag{18}$$

where $I = \frac{8\pi}{15}\rho a^5$ is the particle's moment of inertia, and $\zeta_\mathrm{r} = 8\pi\eta a^3$ is the viscous drag coefficient for particle rotation. Scaling time as $\tau = \omega t$, the dynamics can be non-dimensionalized as

$$\frac{d^2\theta}{d\tau^2} = -\left(\frac{\zeta_\mathrm{r}}{\omega I}\right)\frac{d\theta}{d\tau} - \left(\frac{\mu_0 m_\mathrm{p} H_0}{\omega^2 I}\right)\sin\theta \sin\tau \tag{19}$$

which depends on two dimensionless parameters: $\xi_\mathrm{r}/\omega I$ and $\mu_0 m_\mathrm{p} H_0/\omega^2 I$. Using these parameters, Aranson and co-workers construct a phase-diagram showing the conditions required for spontaneous rolling in the oscillatory field (see Figure 5a of their paper[11]).

For the present experiments, we have polystyrene spheres with density $\rho = 1.05$ g/cm^2 and radius $a = 2.5$ μm immersed in water with viscosity $\eta = 1$ mPa·s. For a typical driving field of magnitude $\mu_0 H_0 = 8$ mT and frequency $f = \omega/2\pi = 40$ Hz, the first parameter is approximated as

$$\frac{\zeta_\mathrm{r}}{\omega I} = \frac{15\eta}{\omega\rho a^2} \approx 0.9 \times 10^4 \tag{20}$$

This value is more than three orders of magnitude larger than that of Aronson and co-workers, who used larger nickel spheres ($a = 60$ μm, $\rho = 8.9$ g/cm^3).

To estimate the second dimensionless parameter for our particles, we use the VSM measurement of $m_\mathrm{p} \approx 8.3 \times 10^{-14}$ A m^2 for the permanent moment. With this estimate, the second dimensionless parameter is even larger than the first, indicating that inertial effects are small relative to both the magnetic torque and the viscous drag

$$\frac{\mu_0 m_\mathrm{p} H_0}{\omega^2 I} \approx 0.6 \times 10^5 \tag{21}$$

Again, this value is considerably larger than that of the Aronson system. The present conditions are not represented on the reported phase diagram, which limit the values of $\zeta_\mathrm{r}/\omega I$ and $\mu_0 m_\mathrm{p} H_0/\omega^2 I$ to 2 and 3, respectively.

6.1 Analysis for vanishing inertia

To assess the possibility of steady rotation, we first non-dimensionalize equation (18) using the characteristic time scale $\omega_0^{-1} = \zeta_\mathrm{r}/\mu_0 m_\mathrm{p} H_0$ to obtain

$$\varepsilon\frac{d^2\theta}{dt} = -\frac{d\theta}{dt} - \sin\theta \sin\omega t \tag{22}$$

where $\varepsilon = \omega_0^2 I/\mu_0 m_\mathrm{p} H_0 \ll 1$ is a small parameter. For simplicity of notation, we use the same variables to denote the dimensionless time $\omega_0 t \to t$ and frequency $\omega/\omega_0 \to \omega$.

We use a perturbation analysis based on multiple scales to derive approximate solutions in the small inertia limit. In this approach, we distinguish a fast time variable $\tau = t$ and a slow time variable $T = \varepsilon t$ and expand the solution as

$$\theta(t, \varepsilon) = \theta_0(\tau, T) + \varepsilon\theta_1(\tau, T) + \mathcal{O}(\varepsilon^2) \tag{23}$$

The total time derivatives in the governing equation are expressed by the following partial derivatives

$$\frac{d\theta}{dt} = \partial_\tau\theta + \varepsilon\partial_T\theta \quad \text{and} \quad \frac{d^2\theta}{dt^2} = \partial_{\tau\tau}\theta + 2\varepsilon\partial_{\tau T}\theta + \varepsilon^2\partial_{TT}\theta \tag{24}$$

Leading order $\mathcal{O}(\varepsilon^0)$. In the overdamped limit of no inertia ($\varepsilon \to 0$), equation (22) simplifies as follows

$$\partial_\tau\theta_0 = -\sin\theta_0 \sin\omega\tau \tag{25}$$

This equation is separable and can be integrated exactly to obtain

$$\theta_0(\tau, T) = 2\arctan\left(A(T)e^{\cos(\omega\tau)/\omega}\right) \tag{26}$$

where $A(T)$ is a function of the slow time variable. The initial condition $\theta(0) = \theta^{\text{ic}}$ implies the following condition at leading order $\mathcal{O}(\varepsilon^0)$

$$\theta_0(0, 0) = \theta^{\text{ic}} = 2\arctan\left(A(0)e^{1/\omega}\right) \quad \Rightarrow \quad A(0) = e^{-1/\omega}\tan(\theta^{\text{ic}}/2) \tag{27}$$

First order correction $\mathcal{O}(\varepsilon)$. At first order in the inertia parameter ε, the governing equation becomes

$$\partial_{\tau\tau}\theta_0 = -\partial_T\theta_0 - \partial_\tau\theta_1 - \theta_1\cos\theta_0\sin\omega\tau \tag{28}$$

Multiplying this equation by the integrating factor $1/\sin\theta_0$ and making use of the zeroth order solution θ_0, we can write simplify this equation as

$$\partial_\tau\left(\frac{\theta_1}{\sin\theta_0}\right) = -\frac{\partial_T\theta_0}{\sin\theta_0} + \omega\cos\omega\tau - \sin^2\omega\tau\cos\theta_0 \tag{29}$$

To ensure that θ_1 is bounded and $2\pi/\omega$-periodic in τ, we require that this equation average to zero over one fast period

$$0 = \left\langle -\frac{\partial_T\theta_0}{\sin\theta_0} + \omega\cos\omega\tau - \sin^2\omega\tau\cos\theta_0 \right\rangle_\tau \tag{30}$$

This solvability condition (30) can be used to derive a differential equation for the function $A(T)$. The zero-order solution (26) implies the identity

$$\frac{\partial_A\theta_0}{\sin\theta_0} = \frac{1}{A} \quad \Rightarrow \quad \frac{\partial_T\theta_0}{\sin\theta_0} = \frac{A'}{A} \tag{31}$$

which is independent of τ. The solvability condition (30) therefore simplifies as

$$A'(T) = -A(T)\left\langle \sin^2\omega\tau\cos\theta_0 \right\rangle_\tau \tag{32}$$

subject to the initial condition (27).

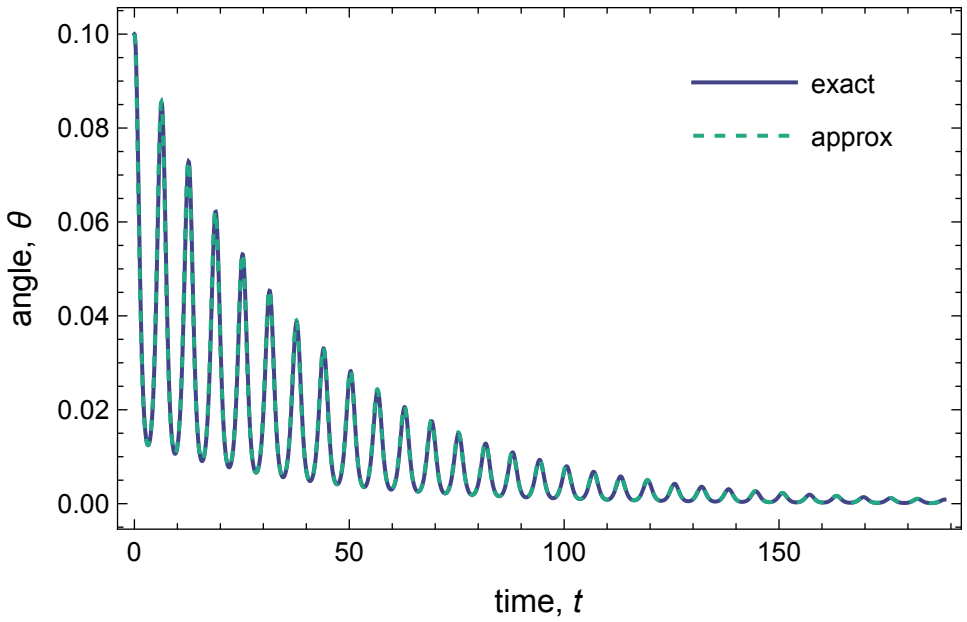

Figure S8: Transient moment angle $\theta(t)$ versus time for $\varepsilon = 0.05$, $\omega = 1$, and $\theta^{\text{ic}} = 0.1$. The solid curve is obtained by numerical integration of equation (22). The dashed curve is the analytical approximation of equation (34).

At long times ($T \to \infty$), the function $A(T)$ approaches zero as the moment angle θ approaches 0. In this limit when $|\theta_0| \ll 1$ and $\cos\theta_0 \approx 1$, equation (32) simplifies as

$$A'(T) = -\tfrac{1}{2}A(T) \quad \Rightarrow \quad A(T) = A(0)e^{-T/2} = A(0)e^{-\varepsilon t/2} \tag{33}$$

The zeroth order solution (26) simplifies as

$$\theta_0(\tau, T) = 2A(T)e^{\cos(\omega\tau)/\omega} \quad \Rightarrow \quad \theta_0(t) = 2A(0)\exp\left(\frac{\cos(\omega t)}{\omega} - \tfrac{1}{2}\varepsilon t\right) \tag{34}$$

Over a time scale $2/\varepsilon$, particle inertia acts to orient the particle's magnetic moment along the direction of the applied field. In addition this this asymptotic solution for $\theta_0 \to 0$, there exists an analogous solution with $\theta_0 \to \pi$, in which the moment points in the negative z-direction. There is no steady rotation of the particle for $\varepsilon \ll 1$. These analytical results are further supported by numerical integration as illustrated in Figure S8 for $\varepsilon = 0.05$ and $\omega = 1$.

To summarize, this model suggests that a ferromagnetic sphere will not rotate steadily in an oscillating field in the low inertia regime, $\varepsilon \ll 1$. Instead, the particle will align its magnetic moment along the axis of the oscillating field on a time scale $2/\varepsilon\omega_0$. For our magnetic Janus spheres, this time scale is estimated to be $\sim$2 s ($\varepsilon \approx 7 \times 10^{-4}$, $\omega_0/2\pi \approx 270$ Hz).

7 3D rotation in an oscillating field

We now consider particle rotation in three dimensions for fast internal relaxation ($k \to \infty$) and negligible inertia ($\varepsilon \to 0$). The Euler angles ϕ, θ, ψ evolve as

$$\begin{aligned}
\dot{\phi} &= (\Omega_x \cos\psi + \Omega_y \sin\psi) \csc\theta \\
\dot{\theta} &= \Omega_y \cos\psi - \Omega_x \sin\psi \\
\dot{\psi} &= -(\Omega_x \cos\psi + \Omega_y \sin\psi) \cot\theta
\end{aligned} \tag{35}$$

where the components of the angular velocity are proportional to the magnetic torque

$$\begin{aligned}
Y_c^{-1}\,\Omega_x &= [\sin\delta \sin(\phi+\gamma)\cos\psi + (\sin\delta\cos(\phi+\gamma)\cos\theta + \cos\delta\sin\theta)\sin\psi]\sin\omega t \\
&\quad - \left[(\Delta_{yz}-\Delta_{xz})\sin 2\phi \sin\theta\cos\psi - (\Delta_{xz} + (\Delta_{yz}-\Delta_{xz})\sin^2\phi)\sin 2\theta \sin\psi\right]\sin^2\omega t \\
Y_c^{-1}\,\Omega_y &= [\sin\delta \sin(\phi+\gamma)\sin\psi - (\sin\delta\cos(\phi+\gamma)\cos\theta + \cos\delta\sin\theta)\cos\psi]\sin\omega t \\
&\quad - \left[(\Delta_{yz}-\Delta_{xz})\sin 2\phi \sin\theta\sin\psi + (\Delta_{xz} + (\Delta_{yz}-\Delta_{xz})\sin^2\phi)\sin 2\theta \cos\psi\right]\sin^2\omega t
\end{aligned} \tag{36}$$

Here, we have parameterized the permanent moment by the polar angle δ and the azimuthal angle γ such that $\mathbf{m}_\mathrm{p} = \cos\gamma\sin\delta\,\mathbf{b}_x + \sin\gamma\sin\delta\,\mathbf{b}_y + \cos\delta\,\mathbf{b}_z$. The two polarizability differences are $\Delta_{xz} = \frac{1}{2}(\alpha_z - \alpha_x) > 0$ and $\Delta_{yz} = \frac{1}{2}(\alpha_z - \alpha_y) > 0$. The angular velocity in the z-direction is identically zero. As in Section 5 above, we can rescaled time as $\tilde{t} = Y_c t$, frequency as $\tilde{\omega} = \omega/Y_c$, and angular velocity as $\tilde{\Omega} = \Omega/Y_c$ to remove the dependence on Y_c from the angular evolution equations.

When the permanent moment lies in the $\mathbf{b}_x$-$\mathbf{b}_z$ plane of the particle (i.e., when $\gamma = 0$), which—by definition—is also the plane of higher polarizability, we recover the 1D rolling model of the previous section. The Janus director $\mathbf{b}_y$ orients perpendicular to the applied field, and the particle rotates about this axis. The addition of a small component of the permanent moment in the $\mathbf{b}_y$ direction breaks this simple 1D rotation, reproducing some of the features observed in experiment.

7.1 In-plane rotation for $\tilde{\omega} > \tilde{\omega}_\mathbf{c}$

Above the critical frequency, the addition of a small component of the permanent moment along the Janus director $\mathbf{d} = \mathbf{b}_y$ can lead to in-plane particle rotation similar to that observed in experiment (Fig. 3e). Figure S9 shows the angular orientation of the in-plane rotation vector $\mathbf{IPR} = \mathbf{d} - (\mathbf{e}_z \cdot \mathbf{d})\mathbf{e}_z$ vs. time for model parameters $\delta = \pi/4$ and $\Delta_{xz} = 0.01$ (as in Fig. S6). Additionally, the average polarizability is $\frac{1}{3}(\alpha_x + \alpha_y + \alpha_z) = 0.4$ (from VSM), the yz polarizability difference is set to $\Delta_{yz} = \frac{1}{2}(\alpha_z - \alpha_y) = 0.2$, the azimuthal angle of the permanent moment is $\gamma = 0.1$ rad, and the driving frequency is $\tilde{\omega} = 0.5$ (ca. three times the critical value). For these conditions, the Janus director remains approximately perpendicular to the $\mathbf{e}_z$ direction of the oscillating field, but rotates back and forth in the xy plane alternating between steady clockwise and counterclockwise rotation. These results suggest that apparent in-plane rotation is possible even in the absence of external torques and angular velocities in the $\mathbf{e}_z$ direction.

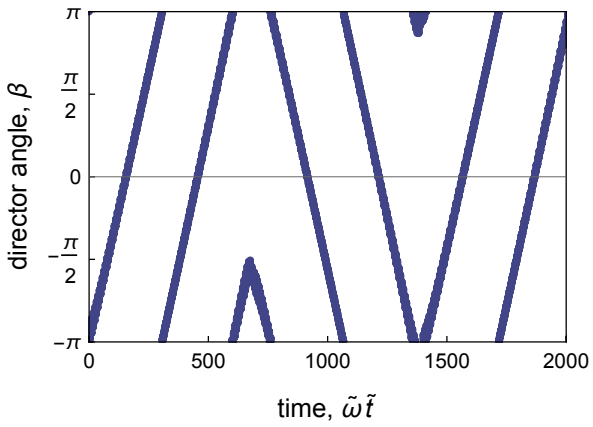

Figure S9: In-plane rotation in an oscillating field as predicted by numerical integration of equations (35) and (36). The angle β measures the orientation of the in-plane rotation vector $\mathbf{IPR} = \mathbf{d} - (\mathbf{e}_z \cdot \mathbf{d})\mathbf{e}_z$ in the xy plane. Dimensionless model parameters are: $\delta = \pi/4$, $\gamma = 0.1$, $\Delta_{xz} = 0.01$, $\Delta_{yz} = 0.2$, $\tilde{\omega} = 0.5$. See also Supplementary Movie 2.

8 Spectral analysis of particle speed

In contrast to torque-driven rolling in a continuously rotating magnetic field, propulsion driven by an out-of-plane oscillating field is predicted to produce temporal oscillations in the particle speed. To test this prediction experimentally, we analyze the frequency content of the particle's instantaneous speed extracted from tracked trajectories.

From tracked centroid coordinates (X_i, Y_i) sampled at times t_i, we compute the frame-to-frame displacement

$$\Delta r_i = \sqrt{(X_i - X_{i-1})^2 + (Y_i - Y_{i-1})^2} \tag{37}$$

and define the scalar speed magnitude v_i at time t_i as

$$v_i = \frac{\Delta r_i}{\Delta t_i} \quad \text{with} \quad \Delta t_i = t_i - t_{i-1} \tag{38}$$

For each experimental condition (driving frequency f and particle height h), we remove the mean (DC) component to isolate the oscillatory contribution to the speed

$$v_i^{\text{osc}} = v_i - \frac{1}{N}\sum_i v_i \tag{39}$$

where N is the number of time steps. Subtracting the mean speed suppresses the non-oscillatory contribution at zero frequency, which would otherwise dominate the spectrum and obscure periodic features near the driving frequency.

We analyze the oscillatory component of the particle speed using its power spectral density (PSD) to identify the dominant temporal modulations. The PSD shows clear peaks at the applied magnetic driving frequency f and at its second harmonic $2f$ (Fig. S10). Consistent with the proposed rotation mechanism, the dominant peak occurs at $2f$, reflecting particle reorientation

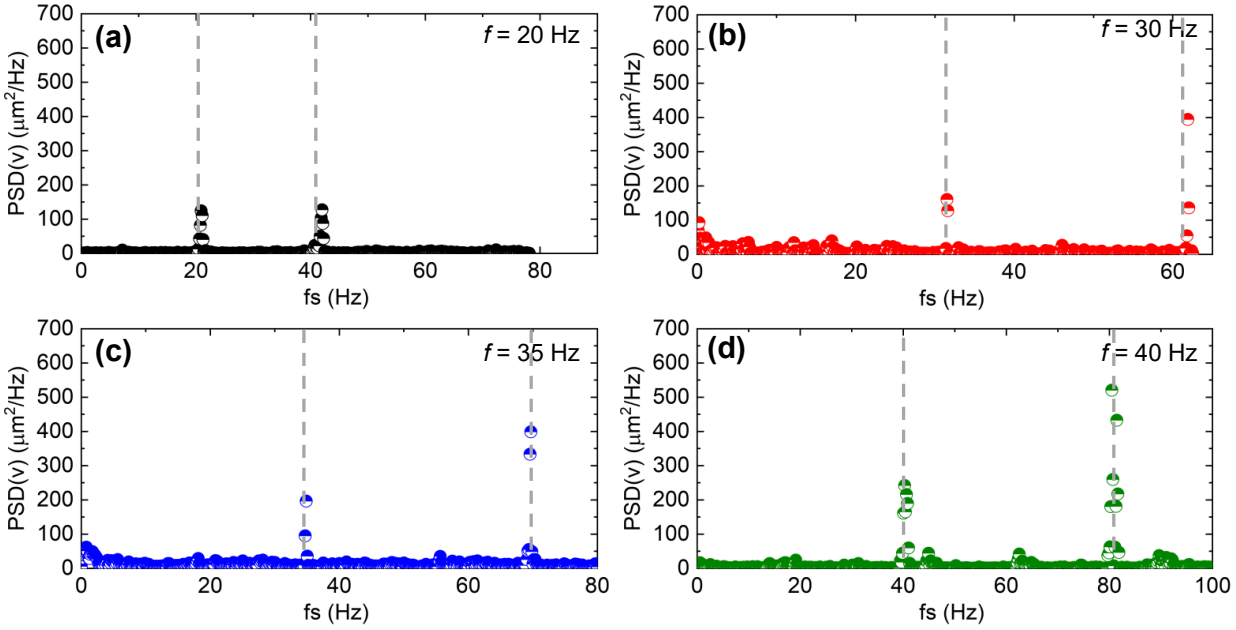

Figure S10: (a-d) Power spectral density PSD(v) of the oscillatory particle speed v_{osc} for hybrid motions measured at magnetic field frequencies $f = 20, 30, 35$, and 40 Hz respectively at $h \sim 18$ μm.

upon each polarity reversal of the oscillatory field. The peak at f is not predicted by the idealized model and likely arises from weak symmetry-breaking effects, such as a small DC component in the applied magnetic field, which breaks the equivalence between the two half-cycles of the oscillatory drive.

9 Polar tilt of Janus patch

We quantify the tilt of the Janus director relative to the imaging direction by measuring the two-dimensional projected area of the metal patch. Image stacks are imported into ImageJ, converted to grayscale, and thresholded to isolate the metallic patch. The patch is a hemispherical cap on a spherical particle of radius a, so its projected area depends only on the out-of-plane tilt angle ϕ and is independent of in-plane rotation. The maximal projected area is $A_{\max} = \pi a^2$. The observed projected area $A(\phi)$ satisfies the conditions

$$A(0) = A_{\max}, \qquad A(\pi/2) = A_{\max}/2, \qquad A(\pi) = 0, \tag{40}$$

corresponding to a fully visible, half-visible, and fully hidden patch, respectively. We approximate the projected area using a simple parametric form that satisfies these conditions

$$\frac{A(\phi)}{A_{\max}} = \frac{1 + \cos\phi}{2} \tag{41}$$

The tilt angle ϕ is estimated by inverting this relation. This approximation captures the leading order dependence of the projected area on tilt and is sufficient for estimating relative changes in ϕ across experimental conditions.

Figure S11 shows the extracted tilt angle $\phi(t)$ for particles at different heights and driving frequencies. The measured tilt remains approximately constant at $\phi \approx \pi/2$ across all conditions, indicating that the metal patch is oriented sideways. These observations are consistent with our conclusion that gravitational torques are much weaker than magnetic torques in setting the particle orientation.

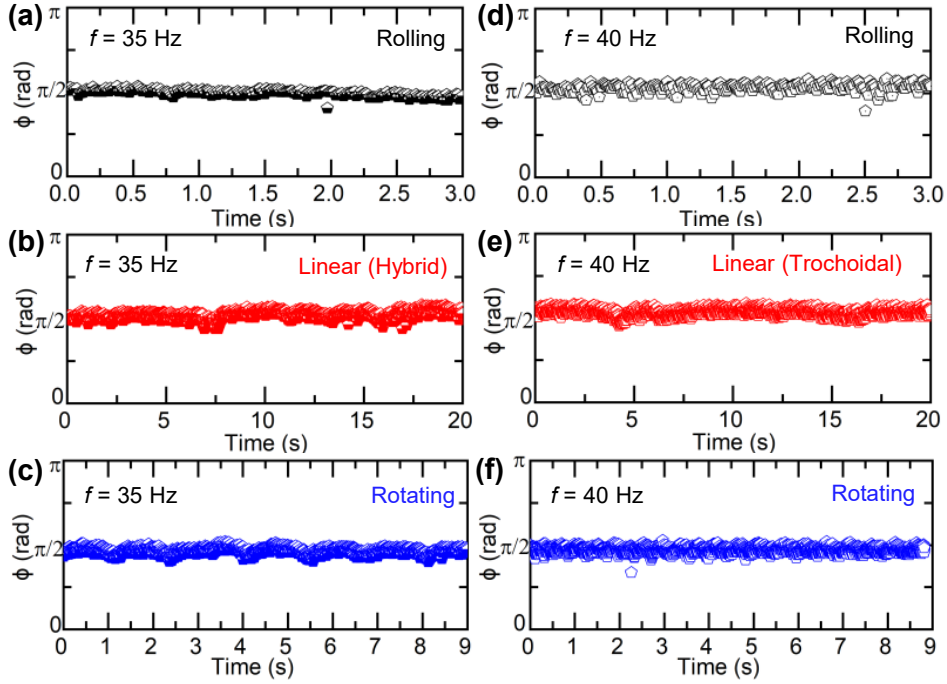

Figure S11: Polar tilt of the metal patch of Janus, ϕ in particle dynamics in Figure 3 of manuscript (a-c) Plot of ϕ vs time at $f = 35$ Hz at $h \sim 2.5$ μ m, $h \sim 18$ μ m, and $h \sim 36$ μ m, respectively. (d-f) Plot of ϕ vs time at $f = 40$ Hz at $h \sim 2.5$ μ m, $h \sim 18$ μm, and $h \sim 36$ μm, respectively.

10 Gravitational torques are small but relevant

The center of mass of a Janus sphere is displaced from its geometric center by the dense magnetic layer deposited onto one hemisphere. To estimate this displacement, we assume line-of-sight deposition of a metal layer with density ρ_m and thickness λ onto a sphere of radius a. The mass of the metal layer is $M_\mathrm{m} = \rho\pi a^2\lambda$. Assuming that $\lambda \ll a$, the center of mass of the deposited metal is shifted from the sphere center by a distance $d_\mathrm{m} = \frac{2}{3}a$ along the Janus director. The torque on the particle in a gravitational field $\mathbf{g} = -g\mathbf{e}_z$ is

$$\mathbf{T}_\mathrm{g} = M_\mathrm{m}\mathbf{d}_\mathrm{m} \times \mathbf{g} \tag{42}$$

which has a characteristic magnitude $M_\mathrm{m}d_\mathrm{m}g = \frac{2\pi}{3}\rho a^3\lambda g$.

To assess the relevance of this torque, we compare to the characteristic magnetic torque $\mu_0 m_\mathrm{p} H_0$ discussed in the previous sections. For an $a = 2.5$ μm Janus sphere with a 20 nm chromium layer (7.19 g/cm^3) and a 22 nm iron layer (7.87 g/cm^3), the metal thickness is $\lambda = 42$ nm with an average density $\rho_\mathrm{m} = 7.5$ g/cm^3. The gravitational torque is estimated to be $T_\mathrm{g} \approx 1.0\times10^{-19}$ N·m. The magnetic torque is estimated to be $\mu_0 m_\mathrm{p} H_0 \approx 6.6\times10^{-16}$ N·m based on VSM data and the applied field strength. The ratio of this estimate to the magnetic torque is $G = M_\mathrm{m}d_\mathrm{m}g/\mu_0 m_p H_0 \approx 1.5\times10^{-4} \ll 1$. Nevertheless, despite its small magnitude, the gravitational torque can influence the trajectory of rolling particles near the surface and contribute to in-plane rotation far from the surface.

With the addition of the gravitational torque, equation (36) for the angular velocities contains additional terms proportional to G

$$\begin{aligned}
Y_c^{-1}\,\Omega_x &= -G\,(\cos\phi\cos\psi - \sin\phi\cos\theta\sin\psi) \\
&\quad + [\sin\delta\sin(\phi+\gamma)\cos\psi + (\sin\delta\cos(\phi+\gamma)\cos\theta + \cos\delta\sin\theta)\sin\psi]\sin\omega t \\
&\quad - \left[(\Delta_{yz}-\Delta_{xz})\sin 2\phi\sin\theta\cos\psi - (\Delta_{xz} + (\Delta_{yz}-\Delta_{xz})\sin^2\phi)\sin 2\theta\sin\psi\right]\sin^2\omega t \\
Y_c^{-1}\,\Omega_y &= -G\,(\cos\phi\sin\psi + \sin\phi\cos\theta\cos\psi) \\
&\quad + [\sin\delta\sin(\phi+\gamma)\sin\psi - (\sin\delta\cos(\phi+\gamma)\cos\theta + \cos\delta\sin\theta)\cos\psi]\sin\omega t \\
&\quad - \left[(\Delta_{yz}-\Delta_{xz})\sin 2\phi\sin\theta\sin\psi + (\Delta_{xz} + (\Delta_{yz}-\Delta_{xz})\sin^2\phi)\sin 2\theta\cos\psi\right]\sin^2\omega t
\end{aligned} \tag{43}$$

Together with equation (35), these equations can be integrated to simulate the orientational dynamics of the Janus sphere.

10.1 In-plane rotation for $\tilde{\omega} < \tilde{\omega}_\mathbf{c}$

Below the critical frequency ($\tilde{\omega} < \tilde{\omega}_\mathrm{c}$), out-of-plane rotation at the driving frequency $\tilde{\omega}$ is accompanied by a slower in-plane rotation due to gravity. Figure S12 illustrates this behavior for model parameters $\delta = \pi/4$ and $\Delta_{xz} = 0.01$ (as in Fig. S6). The permanent moment is assumed to lie in the $\mathbf{b}_x\mathbf{b}_y$ plane of the Janus equator (corresponding to $\gamma = 0$). In the absence of gravity, the critical frequency is $\tilde{\omega}_\mathrm{c} = 0.164$ as described by Figure S7a. With the addition of a small gravity parameter $G = 10^{-4}$, the in-plane rotation angle β increases steadily with time at average rate much slower than the driving frequency: $\langle d\beta/d\tilde{t}\rangle \ll \tilde{\omega}$ (Fig. S12a).

The direction of this in-plane rotation is determined by the "handedness" of the particle. For a "right-handed" particle ($0 < \delta < \pi/2$) that rotates out-of-plane with angular velocity $\hat{\mathbf{\Omega}}\cdot\mathbf{b}_y \approx 1$, the slower in-plane rotation rate is positive (rotation in the positive $\mathbf{e}_z$ direction). By contrast, "left-handed" particles ($-\pi/2 < \delta < 0$) with $\hat{\Omega}\cdot\mathbf{b}_y \approx -1$ rotate in the opposite direction. When rolling across a surface, both right- and left-handed particles turns towards their Janus cap in the direction of travel.

Figure S12b shows the speed of in-plane rotation as a function of the driving frequency $\tilde{\omega}$ for three different values of the gravity parameter G. Below the critical frequency, the IPR speed does not vary strongly with frequency, but increases linearly with the gravity parameter G. For particles moving near a surface, such in-plane rotation leads particles to roll along circular trajectories with a radius of $R = \kappa\tilde{\omega}/\langle d\beta/d\tilde{t}\rangle$. For example, with $\tilde{\omega} = 0.1$, $G = 10^{-4}$, and $\kappa = 0.034$, the radius is predicted to be $R = 1.9$ (in units of particle radii a). This prediction conflicts with experimental observations of linear trajectories; however, different parameter estimates can help to resolve the discrepancy. For example, by increasing the dimensionless polarizability difference Δ_{yz} from 0.2 to 0.6, the trajectory radius increases from $R = 1.9$ to 20.6.

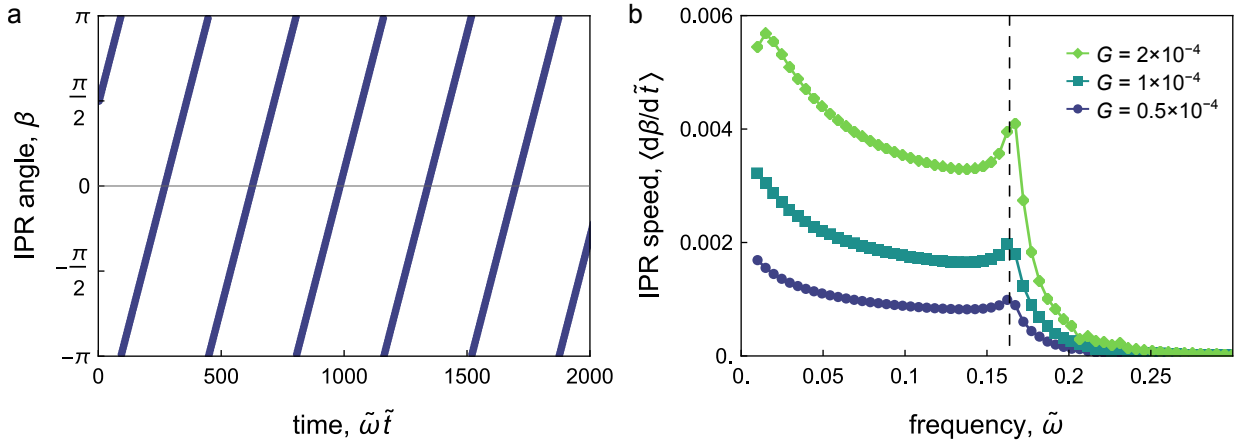

Figure S12: In-plane rotation due to gravitational torques. (a) In-plane rotation angle β vs. time for model parameters: $\delta = \pi/4$, $\gamma = 0$, $\Delta_{xz} = 0.01$, $\Delta_{yz} = 0.2$, $\tilde{\omega} = 0.1$, and $G = 10^{-4}$ (Supplementary Movie 2). (b) Average in-plane rotation rate $\langle d\beta/d\tilde{t}\rangle$ vs. driving frequency $\tilde{\omega}$ for different gravity parameters G. The vertical dashed line denotes the critical frequency for $G = 0$. Other parameters are the same as in (a).

11 Hydrodynamic memory effects

Linear motion. The linear motion of a small rigid sphere of radius a through an unbounded, quiescent fluid due to a time-dependent force $\mathbf{F}(t)$ is given by[12]

$$M_\mathrm{p}\frac{d\mathbf{U}}{dt} = \mathbf{F}(t) - 6\pi\eta a\mathbf{U} - \frac{1}{2}M_\mathrm{f}\frac{d\mathbf{U}}{dt} - 6\pi\eta a^2\int_{-\infty}^{t}\frac{1}{\sqrt{\pi\nu(t-\tau)}}\frac{d\mathbf{U}}{d\tau}d\tau \tag{44}$$

where M_p is the mass of the particle, M_f is the mass of the fluid displaced by the particle, and $\nu = \mu/\rho$ is the kinematic viscosity of the fluid. In addition to the Stokes drag (term 2), this description includes also the added mass (term 3), which describes the extra inertia the particle seems to have when it accelerates in the fluid, and the Basset force (term 4), which accounts for the history-dependent viscous drag arising from the diffusive spread of vorticity shed by the accelerating sphere. These two effects are not included in our models of particle motion detailed in the previous sections.

To estimate the magnitude of these neglected terms, consider that the particle velocity $\mathbf{U}$ oscillates in time with magnitude U and frequency ω. Dividing through by the Stokes drag $6\pi\eta aU$, the inertia terms scale linearly with the Reynolds number $\mathrm{Re} = \omega a^2/\nu$ as

$$\frac{M_\mathrm{p}}{6\pi\eta aU}\frac{d\mathbf{U}}{dt} \sim \frac{2\rho_\mathrm{p}}{9\rho}\mathrm{Re} \quad \text{and} \quad \frac{M_\mathrm{f}}{12\pi\eta aU}\frac{d\mathbf{U}}{dt} \sim \frac{1}{9}\mathrm{Re} \tag{45}$$

At small Reynolds numbers (here, $\mathrm{Re} \sim 10^{-3}$ for $\omega/2\pi = 40$ Hz and $a = 2.5$ μm), these contributions are negligible (see also Section 6). By contrast, the Basset (history) force scales as $\mathrm{Re}^{1/2}$, which while small is considerably larger than the neglected inertial effects

$$\frac{6\pi\eta a^2}{6\pi\eta aU}\int_{-\infty}^{t}\frac{1}{\sqrt{\pi\nu(t-\tau)}}\frac{d\mathbf{U}}{d\tau}d\tau \sim \frac{1}{\sqrt{2}}\mathrm{Re}^{1/2} \tag{46}$$

Rotational motion. A similar analysis applies to the rotational motion of a small sphere in an unbounded, quiescent fluid due to a time-dependent torque $\mathbf{T}(t)$. In addition to the Stokes drag, there is a history-dependent contribution of the form[13]

$$0 = \mathbf{T}(t) - 8\pi\eta a^3\mathbf{\Omega} - \frac{8\pi\eta a^3}{3\sqrt{\pi}}\int_{-\infty}^{t}\left[\frac{1}{s} - \sqrt{\pi}\exp\left(s^2\right)\mathrm{erfc}(s)\right]\frac{d\mathbf{\Omega}}{d\tau}d\tau \tag{47}$$

where $s^2 = \nu(t-\tau)/a^2$. Here, we have neglected the comparatively small inertial contributions. For oscillatory variations in the angular velocity $\mathbf{\Omega}$ with frequency ω, the history term is a factor of $\mathrm{Re}^{1/2} = (\omega a^2/\nu)^{1/2}$ smaller than the drag term.

Particle-wall interactions. Importantly, hydrodynamic memory effects are expected to depend on the particle-wall separation. According to our model of particle rotation, the particle does not rotate steadily but rather in periodic bursts accompanying the changing direction of the oscillating field. The effects of such bursts diffuse through the surrounding fluid reaching the proximal surface on a time scale h^2/ν. Our model of particle rotation based on the pseudo-steady Stokes' equation for low Reynolds number flow assumes that this diffusion rate is fast compared to the driving frequency: $\omega h^2/\nu \ll 1$. For $h = 30$ μm and $\omega/2\pi = 40$ Hz, this dimensionless parameter is $\omega h^2/\nu = 0.2$, which may make non-negligible contributions to the particle's motion. Moreover, as seen above with the effects of gravity (Section 10), even small torques on the particle can influence its in-plane rotation. We hypothesize that history-dependent, particle-wall interactions are responsible for the complex trochoidal trajectories observed in experiment; however, a detailed model reproducing these effects is beyond the scope of the present work.

References

1. Kim, S. & Karrila, S. J. *Microhydrodynamics: principles and selected applications* (Butterworth-Heinemann, 2013).
2. O'Neill, M. E. A slow motion of viscous liquid caused by a slowly moving solid sphere. *Mathematika* **11,** 67–74 (1964).
3. Goldman, A. J., Cox, R. G. & Brenner, H. Slow viscous motion of a sphere parallel to a plane wall—I Motion through a quiescent fluid. *Chem. Eng. Sci.* **22,** 637–651 (1967).
4. Dean, W. R. & O'Neill, M. E. A slow motion of viscous liquid caused by the rotation of a solid sphere. *Mathematika* **10,** 13–24 (1963).
5. Brenner, H. The slow motion of a sphere through a viscous fluid towards a plane surface. *Chem. Eng. Sci.* **16,** 242–251 (1961).
6. Jeffery, G. B. On the steady rotation of a solid of revolution in a viscous fluid. *Proc. London Math. Soc.* **2,** 327–338 (1915).
7. Diebel, J. Representing attitude: Euler angles, unit quaternions, and rotation vectors. *Matrix* **58,** 1–35 (2006).
8. Gao, Y., Sprinkle, B., Springer, E., Marr, D. W. M. & Wu, N. Rolling of soft microbots with tunable traction. *Sci. Adv.* **9,** eadg0919 (2023).
9. Wu, Y., Ramos, A. & Bishop, K. J. M. Self-Guided Navigation of Magnetic Microspheres on Topographic Landscapes. *ACS Appl. Eng. Mater.* **2,** 2479–2487 (2024).
10. Wu, Y., Chen, G., Ramos, A. & Bishop, K. J. M. Programmable rheotaxis of magnetic rollers in time-varying fields. *Soft Matter,* 7344–7353 (2025).
11. Kaiser, A., Snezhko, A. & Aranson, I. S. Flocking ferromagnetic colloids. *Sci. Adv.* **3,** e1601469 (2017).
12. Maxey, M. R. & Riley, J. J. Equation of motion for a small rigid sphere in a nonuniform flow. *Phys. Fluid* **26,** 883–889 (1983).
13. Lei, U., Yang, C. & Wu, K. C. Viscous torque on a sphere under arbitrary rotation. *Appl. Phys. Lett.* **89** (2006).